Monthly Notices
of the
ROYAL ASTRONOMICAL SOCIETY

MNRAS **476,** 2063–2074 (2018) doi:10.1093/mnras/sty392
Advance Access publication 2018 February 14

The effect of extreme ionization rates during the initial collapse of a molecular cloud core

James Wurster,[1]★ Matthew R. Bate[1] and Daniel J. Price[2]

[1]*School of Physics and Astronomy, University of Exeter, Stocker Rd, Exeter EX4 4QL, UK*
[2]*Monash Centre for Astrophysics and School of Physics and Astronomy, Monash University, VIC 3800, Australia*

Accepted 2018 February 12. Received 2018 February 12; in original form 2017 November 27

ABSTRACT

What cosmic ray ionization rate is required such that a non-ideal magnetohydrodynamics (MHD) simulation of a collapsing molecular cloud will follow the same evolutionary path as an ideal MHD simulation or as a purely hydrodynamics simulation? To investigate this question, we perform three-dimensional smoothed particle non-ideal MHD simulations of the gravitational collapse of rotating, one solar mass, magnetized molecular cloud cores, which include Ohmic resistivity, ambipolar diffusion, and the Hall effect. We assume a uniform grain size of $a_{\rm g} = 0.1$ μm, and our free parameter is the cosmic ray ionization rate, $\zeta_{\rm cr}$. We evolve our models, where possible, until they have produced a first hydrostatic core. Models with $\zeta_{\rm cr} \gtrsim 10^{-13}$ s^{-1} are indistinguishable from ideal MHD models, and the evolution of the model with $\zeta_{\rm cr} = 10^{-14}$ s^{-1} matches the evolution of the ideal MHD model within 1 per cent when considering maximum density, magnetic energy, and maximum magnetic field strength as a function of time; these results are independent of $a_{\rm g}$. Models with very low ionization rates ($\zeta_{\rm cr} \lesssim 10^{-24}$ s^{-1}) are required to approach hydrodynamical collapse, and even lower ionization rates may be required for larger $a_{\rm g}$. Thus, it is possible to reproduce ideal MHD and purely hydrodynamical collapses using non-ideal MHD given an appropriate cosmic ray ionization rate. However, realistic cosmic ray ionization rates approach neither limit; thus, non-ideal MHD cannot be neglected in star formation simulations.

Key words: magnetic fields – MHD – methods: numerical – stars: formation.

1 INTRODUCTION

Molecular clouds contain magnetic fields (e.g. Crutcher 1999; Bourke et al. 2001; Heiles & Crutcher 2005; Troland & Crutcher 2008) with low ionization fractions (Mestel & Spitzer 1956) as low as $n_{\rm e}/n_{\rm H_2} = 10^{-14}$ in dense cores (Nakano & Umebayashi 1986a; Umebayashi & Nakano 1990). Prior to star formation, ionization is mostly driven by cosmic rays interacting with the gas and dust, with contributions from radionuclide decay. After a protostar forms, the protostar itself is thermally ionized and ionizes its immediate environment through X-rays. The ionization rate depends on the source, with typical rates for cosmic rays, radionuclide decay, and X-rays given by $\zeta_{\rm cr} \approx 10^{-17}$ s^{-1}exp$(-\Sigma/\Sigma_{\rm cr})$ (Spitzer & Tomasko 1968; Umebayashi & Nakano 1981), $\zeta_{\rm r} \approx 7.6 \times 10^{-19}$ s^{-1} (Umebayashi & Nakano 2009), and $\zeta_{\rm Xr} \approx 9.6 \times 10^{-17}$ s^{-1}exp$(-\Sigma/\Sigma_{\rm Xr})$ (e.g. Igea & Glassgold 1999; Turner & Sano 2008), respectively, where Σ is the surface density of the gas, and $\Sigma_{\rm cr}$ and $\Sigma_{\rm Xr}$ are the characteristic attenuation depths of cosmic rays and X-rays, respectively.

A completely ionized medium is well represented by ideal magnetohydrodynamics (MHD), while a completely unionized fluid embedded in a magnetic field should be well represented by pure hydrodynamics. In a partially ionized medium, non-ideal MHD is required, where the three non-ideal effects are electron–ion/neutral drift (Ohmic resistivity), ion–electron drift (Hall effect), and ion–neutral drift (ambipolar diffusion). Their relative importance depends, amongst other things, on the gas density, number density of charged species (including grains), gas temperature, and magnetic field strength (e.g. Wardle & Ng 1999; Nakano, Nishi & Umebayashi 2002; Tassis & Mouschovias 2007; Wardle 2007; Pandey & Wardle 2008; Keith & Wardle 2014). The Hall effect also depends on the direction of the magnetic field with respect to the rotation axis (e.g. Braiding & Wardle 2012a,b; Tsukamoto et al. 2015a, 2017; Wurster, Price & Bate 2016).

Many studies have modelled the collapse of a molecular cloud to the first or second Larson core (Larson 1969) using non-ideal MHD (e.g. Nakano & Umebayashi 1986b; Fiedler & Mouschovias 1993; Ciolek & Mouschovias 1994; Li & Shu 1996; Mouschovias 1996; Mouschovias & Ciolek 1999; Shu et al. 2006; Duffin & Pudritz 2009; Mellon & Li 2009; Dapp & Basu 2010; Li, Krasnopolsky & Shang 2011; Machida, Inutsuka & Matsumoto 2011; Dapp,

★ E-mail: j.wurster@exeter.ac.uk

Basu & Kunz 2012; Krasnopolsky et al. 2012; Tomida et al. 2013; Tomida, Okuzumi & Machida 2015; Tsukamoto et al. 2015a,b, 2017; Wurster et al. 2016). For efficiency, these studies typically assumed that the dominant ionization source at early times was cosmic ray ionization and that there was no attenuation. Thus, the canonically used cosmic ray ionization rate is $\zeta_{\rm cr} = 10^{-17}\,{\rm s}^{-1}$.

The first three-dimensional models of collapsing magnetized molecular clouds were performed using ideal MHD (e.g. Price & Bate 2007; Hennebelle & Fromang 2008; Duffin & Pudritz 2009; Hennebelle & Ciardi 2009; Commerçon et al. 2010; Seifried et al. 2011), despite ideal MHD being a poor approximation to observed molecular cloud environment. However, these studies provided useful insight into the behaviour of magnetic fields and provided important benchmarks for future studies. These models were effectively fully ionized; thus, what cosmic ray ionization rate would be required to reproduce these results, assuming non-ideal effects MHD were included?

As a rotating molecular cloud collapses, a dense disc forms (e.g. Larson 1972; Tscharnuter 1987). Given a realistic cosmic ray attenuation rate, the centre of the dense disc should be very weakly ionized or completely neutral, forming a magnetic dead zone (Gammie 1996). A very weakly ionized medium can be self-consistently modelled with non-ideal MHD; however, this can be very expensive to run. Thus, at what ionization rate can a medium be treated as purely hydrodynamical?

The goal of this study is to model the early collapse of a rotating, magnetized molecular cloud core using non-ideal MHD to determine at what cosmic ray ionization rates (if any) a purely hydrodynamical or an ideal MHD collapse can be recovered. The free parameter is the cosmic ray ionization rate, $\zeta_{\rm cr}$, which we held constant throughout each simulation. Due to the computational expense when low ionization rates are used, we only model the collapse up to the formation the first hydrostatic core, except in our two lowest ionization rate models, which never evolved out of the isothermal collapse phase. In Wurster, Bate & Price (2018), we examined how the collapse to stellar core formation changes if one assumes cosmic ray ionization rates $\zeta_{\rm cr} \gtrsim 10^{-16}\,{\rm s}^{-1}$.

This paper is organized as follows. In Section 2, we present our numerical methods, and in Section 3 we present our initial conditions and discuss how the initial environment is affected by different cosmic ray ionization rates. In Section 4, we present and discuss our results, and we conclude in Section 5.

2 NUMERICAL METHOD

2.1 Non-ideal MHD

We solve the equations of self-gravitating, non-ideal MHD given by

$$\frac{{\rm d}\rho}{{\rm d}t} = -\rho(\nabla\cdot\boldsymbol{v}), \tag{1}$$

$$\frac{{\rm d}\boldsymbol{v}}{{\rm d}t} = -\frac{1}{\rho}\nabla\left(P\mathbb{I}\right) - \frac{1}{\rho}\nabla\left(\frac{B^2}{2}\mathbb{I} - \boldsymbol{B}\boldsymbol{B}\right) - \nabla\Phi, \tag{2}$$

$$\frac{{\rm d}\boldsymbol{B}}{{\rm d}t} = (\boldsymbol{B}\cdot\nabla)\,\boldsymbol{v} - \boldsymbol{B}\,(\nabla\cdot\boldsymbol{v}) + \left.\frac{{\rm d}\boldsymbol{B}}{{\rm d}t}\right|_{\rm non-ideal} + \left.\frac{{\rm d}\boldsymbol{B}}{{\rm d}t}\right|_{\rm artificial}, \tag{3}$$

$$\nabla^2\Phi = 4\pi G\rho, \tag{4}$$

where ${\rm d}/{\rm d}t \equiv \partial/\partial t + \boldsymbol{v}\cdot\nabla$ is the Lagrangian derivative, ρ is the density, $\boldsymbol{v}$ is the velocity, P is the hydrodynamic pressure, $\boldsymbol{B}$ is the magnetic field (which has been normalized such that the Alfvén velocity is defined as $v_{\rm A} \equiv B/\sqrt{\rho}$ in code units; see Price & Monaghan 2004), Φ is the gravitational potential, G is the gravitational constant, and $\mathbb{I}$ is the identity matrix. The equation set is closed by a barotropic equation of state,

$$P = \begin{cases} c_{\rm s,0}^2\rho; & \rho < \rho_{\rm c}, \\ c_{\rm s,0}^2\rho_{\rm c}\,(\rho/\rho_{\rm c})^{7/5}; & \rho_{\rm c} \le \rho < \rho_{\rm d}, \\ c_{\rm s,0}^2\rho_{\rm c}\,(\rho_{\rm d}/\rho_{\rm c})^{7/5}\,(\rho/\rho_{\rm d})^{11/10}; & \rho \ge \rho_{\rm d}, \end{cases} \tag{5}$$

where $c_{\rm s,\,0}$ is the initial isothermal sound speed, and the density thresholds are $\rho_{\rm c} = 10^{-14}\,{\rm g\,cm^{-3}}$ and $\rho_{\rm d} = 10^{-10}\,{\rm g\,cm^{-3}}$.

The non-ideal MHD term in equation (3) is

$$\left.\frac{{\rm d}\boldsymbol{B}}{{\rm d}t}\right|_{\rm non-ideal} = -\nabla\times\left[\eta_{\rm OR}\,(\nabla\times\boldsymbol{B})\right] \tag{6}$$

$$-\nabla\times\left[\eta_{\rm HE}\,(\nabla\times\boldsymbol{B})\times\hat{\boldsymbol{B}}\right] \tag{7}$$

$$+\nabla\times\left\{\eta_{\rm AD}\left[(\nabla\times\boldsymbol{B})\times\hat{\boldsymbol{B}}\right]\times\hat{\boldsymbol{B}}\right\}, \tag{8}$$

where the non-ideal coefficients for Ohmic resistivity, the Hall effect, and ambipolar diffusion terms are given in (e.g.) Wardle & Ng (1999) and Wardle (2007).

To calculate the number densities of the charged species and thus the non-ideal MHD coefficients, we use Version 1.2.1 of the NICIL library (Wurster 2016). The maximum temperature reached in this study will be $T < 500$ K; thus, cosmic rays will be the only ionization source, since we intentionally ignore ionization from radionuclide decay in order to test the effect of low ionization rates. Cosmic rays can create two species of negatively charged ions: a light ion species based upon hydrogen and helium components and a heavy ion species with the mass of magnesium (e.g. Asplund et al. 2009). We include three species of grains that can absorb free electrons to become negatively charged $n_{\rm g}^-$, or lose electrons through collisions to become positively charged $n_{\rm g}^+$, or remain neutral $n_{\rm g}^0$. The total number density of grains is dependent on the local gas density, namely

$$n_{\rm g} = f_{\rm fg}\frac{m_{\rm n}}{m_{\rm g}}n_{\rm gas}, \tag{9}$$

where $f_{\rm dg}$ is the gas-to-dust ratio, $m_{\rm n}$ and $m_{\rm g}$ are the masses of a neutral particle and dust grain, respectively, and $n_{\rm gas}$ is the gas number density. To conserve gain number density, $n_{\rm g} = n_{\rm g}^- + n_{\rm g}^0 + n_{\rm g}^+$.

2.2 Smoothed particle non-ideal MHD

Our calculations are carried out using the 3D smoothed particle magnetohydrodynamics (SPMHD) code PHANTOM (Price et al. 2017) with the inclusion of self-gravity and non-ideal MHD (Wurster 2016). The density of each smoothed particle hydrodynamics (SPH) particle a is calculated by iteratively solving

$$\rho_a = \sum_b m_b W_{ab}(h_a); \quad h_a = h_{\rm fac}\left(\frac{m_a}{\rho_a}\right)^{1/3} \tag{10}$$

using the Newton–Raphson method, where we sum over all neighbours b, m_a and h_a are the particle's mass and smoothing length, respectively, W_{ab} is the smoothing kernel, and $h_{\rm fac} = 1.2$ is a coefficient required to obtain ∼58 neighbours when using the adopted cubic spline kernel.

The remainder of the discretized SPMHD equations are readily available in the literature (e.g. see review by Price 2012), and we use the same form as given in Wurster et al. (2016). We

enforce the divergence-free condition on the magnetic field using the constrained hyperbolic/parabolic divergence cleaning algorithm described in Tricco & Price (2012) and Tricco, Price & Bate (2016).

In ideal MHD, artificial resistivity is required for magnetic stability (i.e. the final term in equation 3); as per convention, artificial resistivity is included in all of our simulations both for consistency and for the possibility that physical and artificial resistivity are important in different regions. We use the form given by Price & Monaghan (2004, 2005); however, the signal velocity is instead given by $v_{\mathrm{sig},ab} = |\boldsymbol{v}_{ab} \times \hat{\boldsymbol{r}}_{ab}|$ (Price et al. 2017). A comparison of artificial resistivity algorithms presented in Wurster et al. (2017a) showed that the method used here is the least dissipative of all SPMHD algorithms used to date, especially during the collapse to form the first core. Hence, our results are dominated by physical and not artificial resistivity.

2.3 Time-stepping

In ideal MHD, the limiting time-step for particle a is typically the Courant–Friedrichs–Lewy (CFL) condition,

$$\mathrm{d}t_{\mathrm{CFL},a} = \frac{C_{\mathrm{CFL}} h_a}{\sqrt{c_{\mathrm{s},a}^2 + v_{\mathrm{A},a}^2}}, \tag{11}$$

where $C_{\mathrm{CFL}} = 0.3 < 1.0$ is the dimensionless Courant number and $c_{\mathrm{s},a}$ is the sound speed. However, non-ideal effects each add a new time constraint, namely

$$\mathrm{d}t_{\mathrm{OR},a} = \frac{C_{\mathrm{NI}} h_a^2}{\eta_{\mathrm{OR},a}}, \quad \mathrm{d}t_{\mathrm{HE},a} = \frac{C_{\mathrm{NI}} h_a^2}{|\eta_{\mathrm{HE},a}|}, \quad \mathrm{d}t_{\mathrm{AD},a} = \frac{C_{\mathrm{NI}} h_a^2}{\eta_{\mathrm{AD},a}}, \tag{12}$$

where $C_{\mathrm{NI}} = 1/2\pi$ is a dimensionless coefficient analogous to the Courant number. Test cases with ambipolar diffusion show that the non-ideal MHD time-step can be ∼40–50 shorter than the CFL time-step (e.g. Mac Low et al. 1995; Wurster, Price & Ayliffe 2014); however, in realistic problems, the minimum non-ideal MHD time-step can be several hundred times shorter in quickly evolving, dense regions.

Super-time-stepping (Alexiades, Amiez & Gremaud 1996) is used to relax the conditions given by equation (12) for the diffusive terms that are parabolic in nature (i.e. Ohmic resistivity and ambipolar diffusion). This involves taking $N_{\mathrm{sts}} < N_{\mathrm{real}} \approx \mathrm{d}t_{\mathrm{CFL}}/\min(\mathrm{d}t_{\mathrm{OR}}, \mathrm{d}t_{\mathrm{AD}})$ steps of $\mathrm{d}\tau_j$, where $j = 1, \ldots, N_{\mathrm{sts}}$ and $\mathrm{d}\tau_j > \mathrm{d}\tau_{j+1}$ and requiring stability only at the end of N_{sts} steps rather than at the end of every step. The best possible speed-up yields (e.g. Choi, Kim & Wiita 2009)

$$N_{\mathrm{sts}} = \mathrm{int}\left[\sqrt{\frac{\mathrm{d}t_{\mathrm{CFL}}}{k \cdot \min(\mathrm{d}t_{\mathrm{OR}}, \mathrm{d}t_{\mathrm{AD}})}}\right] + 1, \tag{13}$$

where we set $k = 0.9$. For added stability, we first subdivide $\mathrm{d}t_{\mathrm{CFL}}$ by positive integer n such that $20\mathrm{d}\tau_1 \gtrsim \mathrm{d}t_{\mathrm{CFL}}/n$ and then take $nN_{\mathrm{sts}} < N_{\mathrm{real}}$ steps per $\mathrm{d}t_{\mathrm{CFL}}$; this subdivision by n is only required in extreme environments where multiple physical processes are simultaneously contributing to a complex evolution, or for very low ionization rates (i.e. $\zeta_{\mathrm{cr}} \lesssim 10^{-24}\,\mathrm{s}^{-1}$).

Given the hyperbolic nature of the Hall effect, we are required to solve this time-step explicitly. Methods (e.g. O'Sullivan & Downes 2007; Meyer, Balsara & Aslam 2012) have been proposed to sub-step with the Hall term, but these have yet to be implemented into PHANTOM.

3 INITIAL CONDITIONS

Our models are similar to those used in our previous studies (Price & Bate 2007; Bate, Tricco & Price 2014; Wurster et al. 2016) and consist of a spherical cloud of radius $R = 4 \times 10^{16}$ cm = 0.013 pc and density $\rho_0 = 7.43 \times 10^{-18}$ g cm^{-3} that is placed inside a low-density box of edge length $l = 4R$ and a density contrast of 30:1; the cloud and surrounding medium are in pressure equilibrium. This allows the cloud to be modelled self-consistently, and we use quasi-periodic boundary conditions at the edge of the box, in which SPH particles interact magnetohydrodynamically 'across the box', but not gravitationally. Our simulations use 10^6 particles in the sphere, which are initialized on a regular close-packed lattice.

The initial cloud has mass $M = 1\ \mathrm{M}_\odot$, rotational velocity $\Omega = 1.77 \times 10^{-13}$ rad s^{-1}, and sound speed $c_{\mathrm{s},0} = 2.19 \times 10^4$ cm s^{-1} (i.e. $T_0 = 13.5$ K). We thread the cloud with a uniform magnetic field that is anti-aligned with the axis of rotation, i.e. $\boldsymbol{B} = -B_0\hat{\boldsymbol{z}}$, which will promote disc formation in the presence of the Hall effect (e.g. Braiding & Wardle 2012a,b; Tsukamoto et al. 2015a; Wurster et al. 2016); this configuration yields $(\nabla \times \boldsymbol{B}_0)_0 = 0$. The magnetic field has an initial strength of $B_0 = 1.63 \times 10^{-4}$ G, which corresponds to a normalized mass-to-flux ratio of $\mu_0 \equiv (M/\Phi_{\mathrm{B}})_0/(M/\Phi_{\mathrm{B}})_{\mathrm{crit}} = 5$, where $(M/\Phi_{\mathrm{B}})_0 \equiv M/\left(\pi R^2 B\right)$ is the initial mass-to-flux ratio and $(M/\Phi_{\mathrm{B}})_{\mathrm{crit}} = c_1/(3\pi)\sqrt{5/G}$ is the critical value where magnetic fields prevent gravitational collapse altogether; M is the total mass contained within the cloud, Φ_{B} is the magnetic flux threading the surface of the (spherical) cloud at radius R assuming a uniform magnetic field of strength B, G is the gravitational constant, and $c_1 \simeq 0.53$ is a parameter numerically determined by Mouschovias & Spitzer (1976). The free-fall time is $t_{\mathrm{ff}} = 2.4 \times 10^4$ yr, which is the characteristic time-scale for this study.

The non-ideal MHD models use the default values included in the NICIL library (Wurster 2016). The dust grains have a radius and bulk density of $a_{\mathrm{g}} = 0.1\ \mu$m and $\rho_{\mathrm{b}} = 3$ g cm^{-3} (Pollack et al. 1994), respectively, and the dust-to-gas ratio is $f_{\mathrm{dg}} = 0.01$. The mass of the neutral particle is based upon the hydrogen and helium abundance; thus, $m_{\mathrm{n}} = 2.31\ \mathrm{m_p}$, where $\mathrm{m_p}$ is the mass of a proton. We test 15 cosmic ray ionization rates in the range $\zeta_{\mathrm{cr}} \in [10^{-30}, 10^{-10}]$ s^{-1}, which are indicated by the vertical lines in Fig. 1. Our models will be named after their ionization rate such that model ζ_X has a cosmic ray ionization rate of $\zeta_{\mathrm{cr}} = 10^{-X}\,\mathrm{s}^{-1}$. The ideal MHD and purely hydrodynamical models will be referred to as iMHD and HD, respectively.

Since the time constraint imposed by non-ideal MHD quickly becomes prohibitively expensive for low ionization rates, our focus is on comparing the very early phases of the collapses, typically just prior to or just after entering the first hydrostatic core phase, which begins at $\rho_{\mathrm{max}} \approx 10^{-13}$ g cm^{-3}. The maximum density analysed in this study is $\rho_{\mathrm{max}} \approx 10^{-11}$ g cm^{-3}; however, several of the low ionization rate models end at $\rho_{\mathrm{max}} \lesssim 10^{-14}$ g cm^{-3}.

3.1 Initial behaviour of the charged species and non-ideal MHD coefficients

Fig. 1 shows the species number densities and the non-ideal MHD coefficients, calculated using our initial conditions. At constant density, temperature, and magnetic field strength, the number densities and non-ideal MHD coefficients are strongly dependent on the cosmic ionization rate, ζ_{cr}.

At ionization rates of $\zeta_{\mathrm{cr}} \lesssim 10^{-24}\,\mathrm{s}^{-1}$, cosmic rays are unable to ionize ions rapidly enough for the ions and electrons to significantly

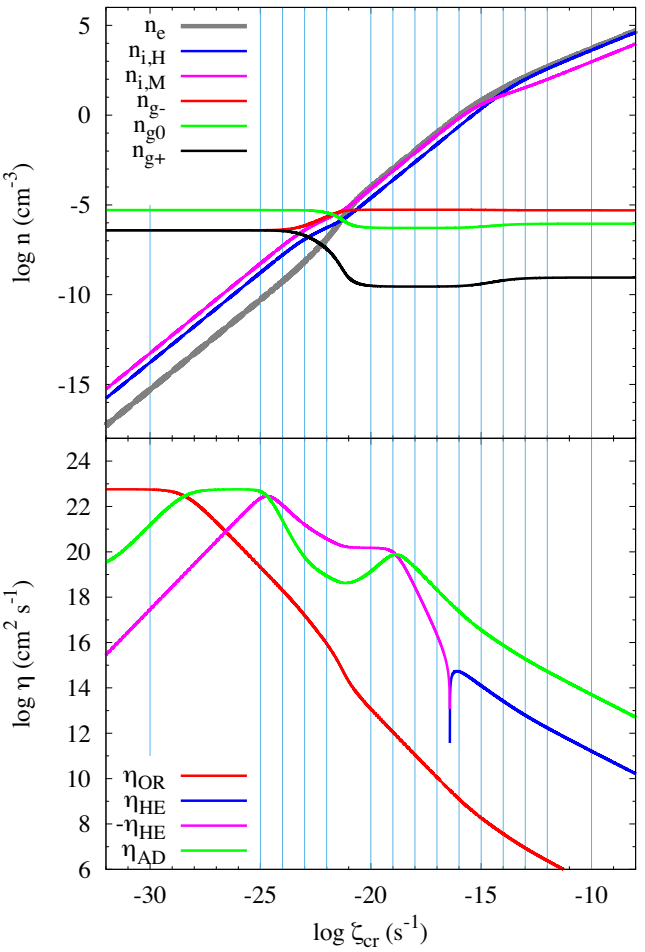

Figure 1. The species number densities (top) and non-ideal MHD coefficients η (bottom) calculated using our initial conditions of $\rho_0 = 7.43 \times 10^{-18}$ g cm^{-3}, $B_0 = 1.63 \times 10^{-4}$ G (i.e. $\mu_0 = 5$), and $c_{s,0} = 2.19 \times 10^4$ cm s^{-1} (i.e. $T_0 = 13.5$ K). The vertical lines represent the values of the cosmic ray ionization rate, ζ_{cr}, that are included in our suite. The grain populations are the dominant species at low ionization rates, and the positively charged ions and electrons are dominant at high ionization rates. This turnover is reflected in η, where $\eta_{AD} < |\eta_{HE}|$. Increasing ζ_{cr} does not lead to a monotonic change in η; thus, models with different initial values of ζ_{cr} will start with different non-ideal effects controlling the evolution.

contribute to the charged species populations; at these rates, the charged species are from grain collisions that transfer electrons to make a positively and negatively charged grain population, with $n_g^- \approx n_g^+$. At ionization rates of $\zeta_{cr} \gtrsim 10^{-20}$ s^{-1}, the ion and electron populations are several orders of magnitude more populous than the charged grain number densities. However, the grains have a much larger mass than the ions (i.e. $m_g = 7.5 \times 10^9\,m_p$ compared to $m_{lightion} = 2.31\,m_p$ and $m_{heavyion} = 24.3\,m_p$), thus still contribute non-trivially to the value of the non-ideal MHD coefficients even at very high ionization rates.

For $\zeta_{cr} \gtrsim 10^{-20}$ s^{-1} (recall that the canonical cosmic ionization rate is $\zeta_{cr} = 10^{-17}$ s^{-1}), the number densities of ions and electrons are similar, and the ionization fraction reaches $n_{e,i}/(n_n + n_i) \approx 0.003$ at $\zeta_{cr} \approx 10^{-10}$ s^{-1}; thus, even at high cosmic ray ionization rates, thermal ionization or another source is required to fully ionize the medium.

Using our given initial conditions, the initial non-ideal MHD coefficients have six regimes:

(i) $\zeta_{cr}/\mathrm{s}^{-1} \lesssim 4 \times 10^{-29}$: $\eta_{OH} > \eta_{AD} > -\eta_{HE}$;
(ii) $4 \times 10^{-29} \lesssim \zeta_{cr}/\mathrm{s}^{-1} \lesssim 3 \times 10^{-27}$: $\eta_{AD} > \eta_{OR} > -\eta_{HE}$;
(iii) $3 \times 10^{-27} \lesssim \zeta_{cr}/\mathrm{s}^{-1} \lesssim 2 \times 10^{-25}$: $\eta_{AD} > -\eta_{HE} > \eta_{OR}$;
(iv) $2 \times 10^{-25} \lesssim \zeta_{cr}/\mathrm{s}^{-1} \lesssim 1 \times 10^{-19}$: $-\eta_{HE} > \eta_{AD} > \eta_{OR}$;
(v) $1 \times 10^{-19} \lesssim \zeta_{cr}/\mathrm{s}^{-1} \lesssim 4 \times 10^{-17}$: $\eta_{AD} > -\eta_{HE} > \eta_{OR}$;
(vi) $4 \times 10^{-17} \lesssim \zeta_{cr}/\mathrm{s}^{-1}$: $\eta_{AD} > \eta_{HE} > \eta_{OR}$.

Although ambipolar diffusion is typically the dominant effect, the Hall effect is the dominant term in region (iv), which is the same region where grains transition from higher number densities compared to the ions to lower number densities. At very low ionization rates, the Ohmic coefficient is approximately constant, since it is dependent on the Ohmic conductivity σ_O, which is approximately constant due to the grain number densities. The Hall coefficient rapidly decreases at low ionization rates due to its dependence on the Hall conductivity σ_H, which will rapidly decrease for $n_g^- \approx n_g^+ \gg n_i$. The ambipolar coefficient is also dependent on the Hall conductivity, but via the perpendicular conductivity, hence its delayed decrease. At high ionization rates, all three terms decrease rapidly as the cloud becomes more ionized. Thus, all three terms have less of an effect on the evolution of the cloud in an absolute sense.

These results are qualitatively similar to those that are obtained from using different ρ_0, B_0, and T_0. Therefore, the numerical results will necessarily differ if we change our initial conditions; however, our qualitative results will be independent of them.

3.2 Grain properties

Although a uniform grain size is not realistic, they are common in numerical models. We use the uniform grain size of $a_0 = 0.1$ μm to match our previous studies (Wurster, Price & Bate 2016, 2017b; Wurster et al. 2018) and to agree with the fiducial value suggested by Pollack et al. (1994). Uniform grain sizes of smaller radius were used in Tsukamoto et al. (2015a,b, 2017).

An alternative to the uniform grain size is the Mathis, Rumpl & Nordsieck (1977, MRN) grain distribution,

$$\frac{\mathrm{d}n_g(a)}{\mathrm{d}a} = A n_H a^{-3.5}, \tag{14}$$

where n_H is the number density of the hydrogen nucleus, $n_g(a)$ is the number density of grains with a radius smaller than a, and $A = 1.5 \times 10^{-25}$ cm$^{2.5}$ (Draine & Lee 1984). In this distribution, there are more grains with smaller radii; thus, the smaller grains will more strongly influence the evolution than the larger grains. Fig. 2 shows the non-ideal MHD coefficients as a function of ζ_{cr} using a uniform grain size of $a_0 = 0.01$ and 1 μm (top two panels), and using the MRN grain distribution using the ranges suggested in Kunz & Mouschovias (2009) and Wardle & Ng (1999; bottom two panels, respectively).

At high ionization rates ($\zeta_{cr} \gtrsim 10^{-13}$ s^{-1}), the coefficients differ by less than 10 per cent, except for $a_0 = 0.1$ μm where the 10 per cent agreement is only for $\zeta_{cr} \gtrsim 10^{-10}$ s^{-1}. Thus, for high ionization rates, we expect the grain properties to play a minimal role in the evolution of the system. As ζ_{cr} decreases to realistic rates ($\zeta_{cr} \approx 10^{-17}$ s^{-1}), the coefficients become more dependent on the grain properties, although the coefficients for our fiducial grain size and the MRN distribution using the Kunz & Mouschovias (2009) range differ by less than a factor of 1.3.

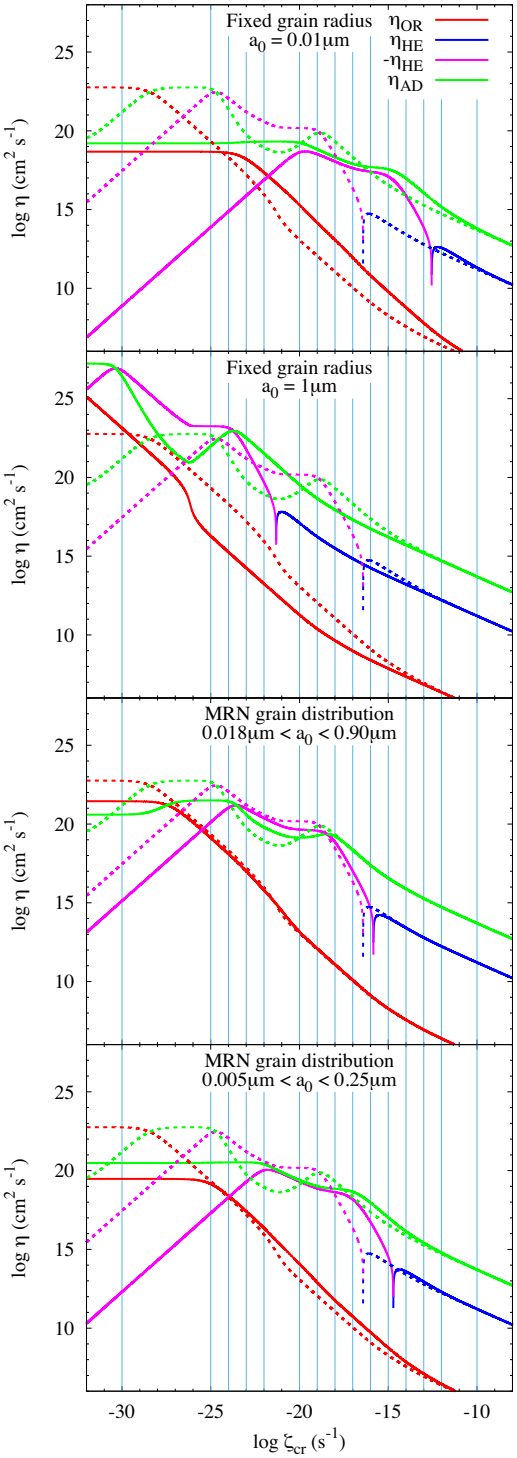

Figure 2. The non-ideal MHD coefficients using our initial conditions as in the bottom panel of Fig. 1. The dotted lines in each panel are calculated using our fiducial uniform grain size of $a_0 = 0.1$ μm, and the solid lines are calculated using the grain size/distribution listed in the panel. The MRN distribution is calculated assuming 40 bins of equal width in log-space. The coefficients have a greater dependence on grain properties at lower cosmic ray ionization rates, where the coefficients can differ by up to 9 dex; at high ionization rates ($\zeta_{\rm cr} \gtrsim 10^{-13}\,{\rm s}^{-1}$), the coefficients typically differ by less than 10 per cent.

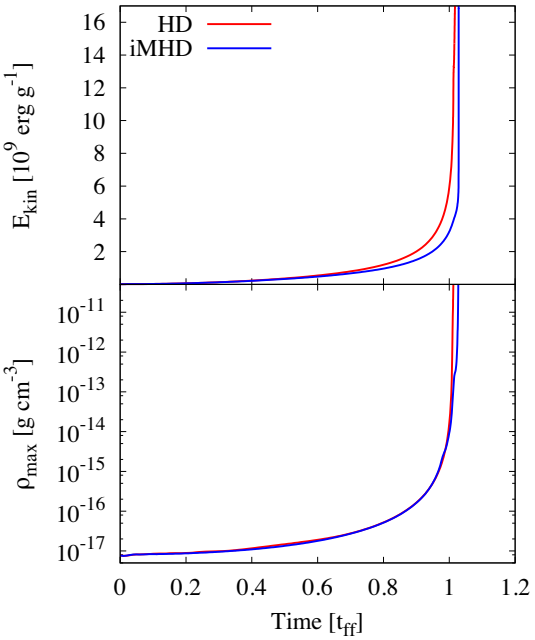

Figure 3. The evolution of the total kinetic energy (top) and the maximum density (bottom) for the HD and iMHD models. The kinetic energy differs by more than 10 per cent for $t \gtrsim 0.51 t_{\rm ff}$, and the maximum density differs by more than 10 per cent at $t \gtrsim 0.99\ t_{\rm ff}$.

At low ionization rates ($\zeta_{\rm cr} \lesssim 10^{-25}\,{\rm s}^{-1}$), the coefficients can differ by up to nine orders of magnitude. For $a_0 = 1$ μm, the coefficients are larger than using our fiducial grain size, suggesting that these systems will approach the hydrodynamical limit at higher ionization rates due to greater non-ideal MHD effects. For $a_0 = 0.01$ μm and the MRN distributions, the coefficients are typically lower than for our fiducial grain size suggesting that these models will be slightly more ideal than our fiducial models. Given that the MRN distributions are the more realistic models, the results we present in Section 4.4 will be upper limits such that using the MRN distribution would require even lower ionization rates to approximate the hydrodynamical case than models using our fiducial uniform grain size of $a_0 = 0.1$ μm.

4 RESULTS

4.1 Limiting models: hydrodynamic and ideal MHD

The iMHD and HD models represent the limiting models such that the models are totally ionized and totally neutral, respectively. Fig. 3 shows their evolution of the total kinetic energy and the maximum density.

Qualitatively, both models follow similar trends, with a slow evolution until $t \approx t_{\rm ff}$, at which time the collapse occurs very rapidly. The presence of strong magnetic fields delays the collapse of the molecular cloud, such that, by $t \approx 0.99\ t_{\rm ff}$, the maximum densities differ by 10 per cent, and it then takes iMHD $\sim$ 370 yr longer to reach $\rho_{\rm max} \approx 10^{-11}$ g cm^{-3} than HD.

The kinetic energy begins to diverge almost immediately with it differing by 10 per cent after $t \approx 0.51\ t_{\rm ff}$, with more kinetic energy in HD than in iMHD at any given time. This is expected since the magnetic field supports the cloud against gravitational collapse; thus, the gas collapses slightly slower.

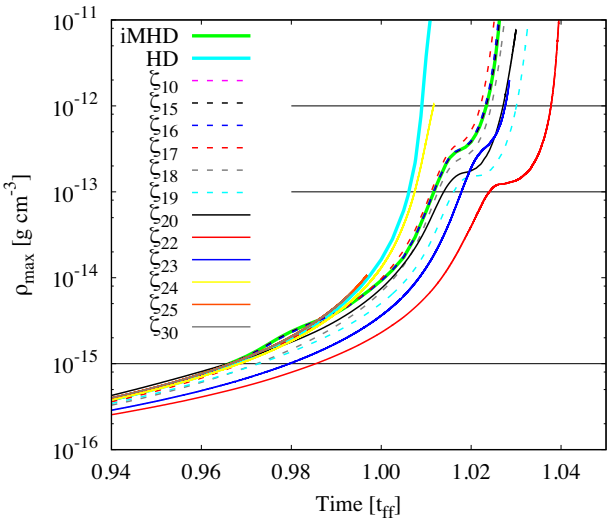

Figure 4. The evolution of the maximum density for selected models for $t > 0.94t_{\rm ff}$. The thick green and cyan lines represent models iMHD and HD, respectively, whose full evolution is shown in the bottom panel of Fig. 3. Models with $\zeta_{\rm cr} \gtrsim 10^{-16}\,{\rm s}^{-1}$ all lie on top of the iMHD curve; thus, only two have been shown for clarity. Model ζ_{17} evolves slightly faster than iMHD, while ζ_{18}–ζ_{23} evolve slower. The low ionization rate models with $\zeta_{\rm cr} \lesssim 10^{-24}\,{\rm s}^{-1}$ evolve similarly to HD. The maximum densities for HD and ζ_{22}–ζ_{30} do not coincide with the centre of the core. Not all models have reached $\rho_{\rm max} = 10^{-11}$ g cm^{-3} due to computational limitations. The horizontal lines match the maximum densities shown in Figs 5–8.

4.2 Transition models: non-ideal MHD

We define any model that includes non-ideal MHD as a transition model since the ionization fraction is neither one (iMHD) nor zero (HD). Fig. 4 shows the late evolution ($t > 0.94t_{\rm ff}$) of the maximum density for selected models, and Figs 5–8 show cross-sections of the density, magnetic field strength, radial and azimuthal velocities of selected models at $\rho_{\rm max} \approx 10^{-15}$, 10^{-13}, and 10^{-12} g cm^{-3}.

The models with $\zeta_{\rm cr} \gtrsim 10^{-16}\,{\rm s}^{-1}$ evolve similarly to iMHD and will be discussed in more detail in Section 4.3 below. These clouds are magnetically supported, thus form a dense collimated structure with strong magnetic fields, since initially, the gas is free to collapse along the rotation axis. The models with $\zeta_{\rm cr} \lesssim 10^{-24}\,{\rm s}^{-1}$ follow a similar evolutionary path as HD and will be discussed in Section 4.4. These models follow an initially spherical collapse; however, by $\rho_{\rm max} > 10^{-13}$ g cm^{-3}, a thick, rotationally supported disc has formed. Throughout their evolution, they retain an approximately uniform magnetic field.

Models ζ_{16} to ζ_{24} do not represent a smooth transition between the evolutionary paths of iMHD and HD as the initial ionization rate is decreased, with the exception of the magnetic field strength and geometry. Agreeing with intuition, ζ_{17} evolves similarly to but slightly faster than iMHD, thus is in the region bracketed by iMHD and HD in Fig. 4. As expected, at our selected $\rho_{\rm max}$ snapshots, its central gas distribution is more diffuse and has a weaker magnetic field strength than the models with $\zeta_{\rm cr} \gtrsim 10^{-16}\,{\rm s}^{-1}$.

The models with $10^{-23} \lesssim \zeta_{\rm cr}/{\rm s}^{-1} \lesssim 10^{-18}$ evolve slower than iMHD, with ζ_{22} having the longest evolutionary time. This is a result of the Hall effect. At these early times, the rotation is beginning to convert the poloidal magnetic field, $|B_{\rm p}| = \sqrt{B_{\rm r}^2 + B_{\rm z}^2}$, into a toroidal magnetic field, $|B_\phi|$. Since the field lines remain closed, there are both $\pm B_\phi \hat{\boldsymbol{\phi}}$ components, and the Hall effect enhances one component and decreases the other. At this stage, the initial direction of the magnetic field is relatively unimportant for the characteristics that we investigate, and we find that models initialized with $\boldsymbol{B} = +B_0\hat{\boldsymbol{z}}$ collapse only slightly faster than their counterparts with $-B_0\hat{\boldsymbol{z}}$, but still do not collapse faster than iMHD. By $\rho_{\rm max} \approx 10^{-12}$ g cm^{-3}, a weak counter-rotating envelope has formed in ζ_{18} and ζ_{19}, and we have verified that this does not form for the $\boldsymbol{B} = +B_0\hat{\boldsymbol{z}}$ models.

Fig. 9 shows the maximum magnetic field strength and the magnitude of the maximum toroidal field as a function of maximum density $\rho_{\rm max}$, which we use as a proxy for time; recall that $B_{\phi,\,0} = 0$.

Although the absolute value of the Hall effect is not the strongest in ζ_{22} (i.e. there are larger values of $|\eta_{\rm HE}|$ at lower ionization rates; see Fig. 1), the net magnetic field in this model is stronger than in ζ_{25} (i.e. the model with the largest $|\eta_{\rm HE}|$) since that model has large ambipolar diffusion. Thus, more of the net magnetic field is

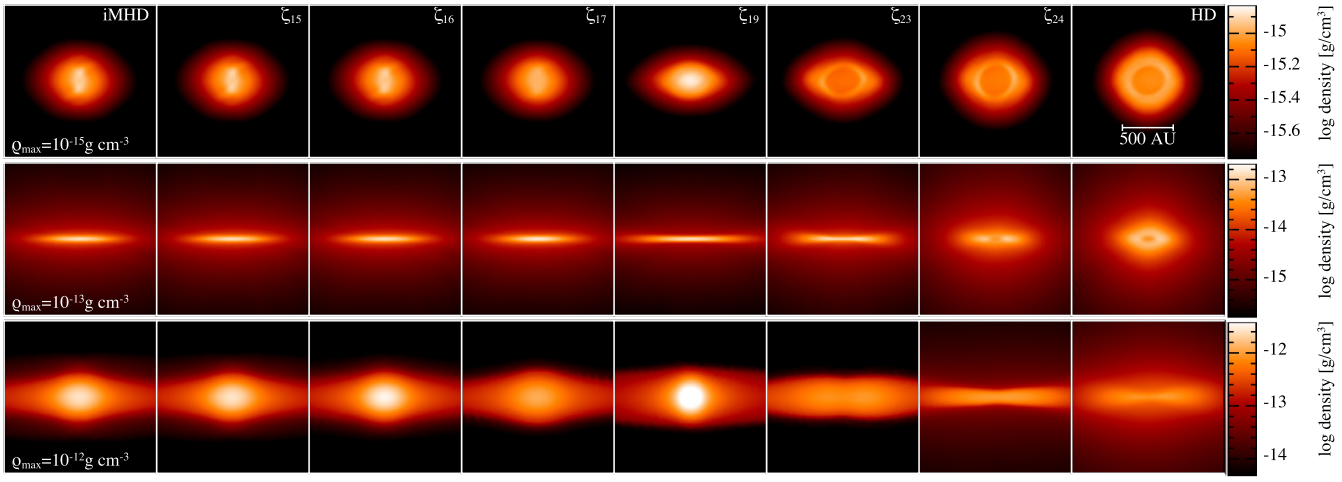

Figure 5. Density slice through the core of the clouds of selected models at $\rho_{\rm max} \approx 10^{-15}$, 10^{-13}, and 10^{-12} g cm^{-3}. Frame sizes and colour bar range change with each row to better show the structure at each $\rho_{\rm max}$. At $\rho_{\rm max} \approx 10^{-15}$ g cm^{-3}, a dense column of gas has formed along the rotation axis in the higher ionization rate models ($\zeta_{\rm cr} \gtrsim 10^{-17}\,{\rm s}^{-1}$), an oblate spheroid has formed for mid-range ionization rates, and the collapse is approximately spherical for low ionization rates ($\zeta_{\rm cr} \lesssim 10^{-23}\,{\rm s}^{-1}$); the maximum density is not in the core for the models with $\zeta_{\rm cr} \lesssim 10^{-22}\,{\rm s}^{-1}$. At $\rho_{\rm max} \approx 10^{-13}$ g cm^{-3}, the scale height of the discs decreases from iMHD to ζ_{22} and then increases again.

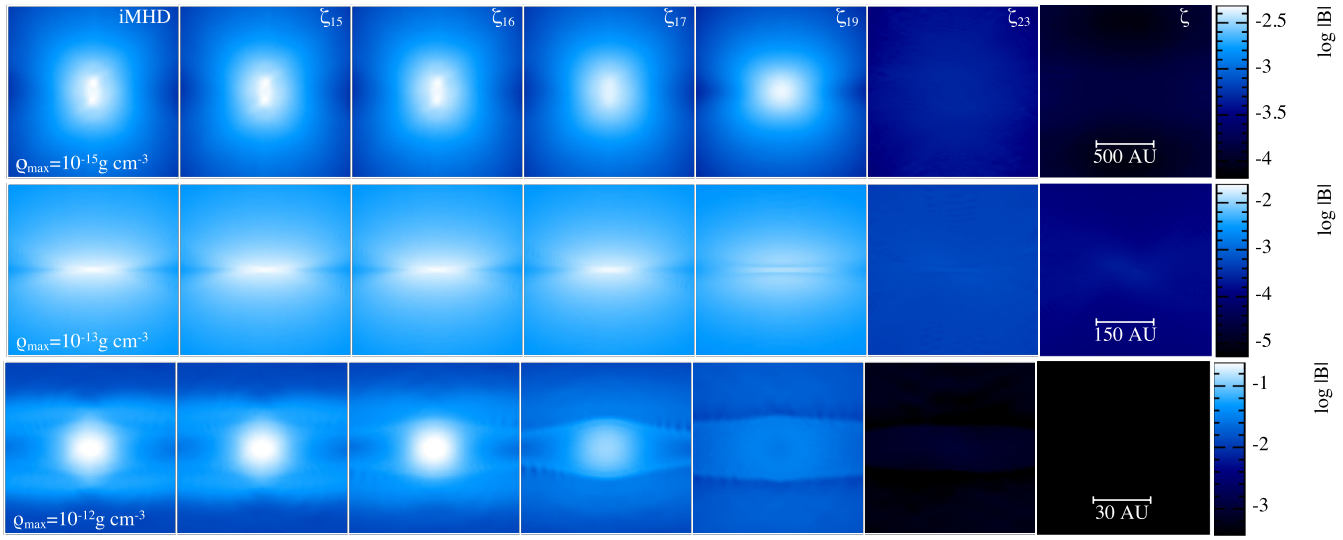

Figure 6. Magnetic field strength through the core of the clouds of selected models as in Fig. 5. At $\rho_{\rm max} \approx 10^{-15}$ g cm^{-3}, the dense column of gas has an enhanced magnetic field strength in the higher ionization rate models ($\zeta_{\rm cr} \gtrsim 10^{-17}$ s^{-1}), while the magnetic field strength is approximately uniform at low ionization rates ($\zeta_{\rm cr} \lesssim 10^{-23}$ s^{-1}). By $\rho_{\rm max} \approx 10^{-12}$ g cm^{-3}, the models with $\zeta_{\rm cr} \lesssim 10^{-19}$ s^{-1} have an unstructured magnetic field that is stronger in the mid-plane.

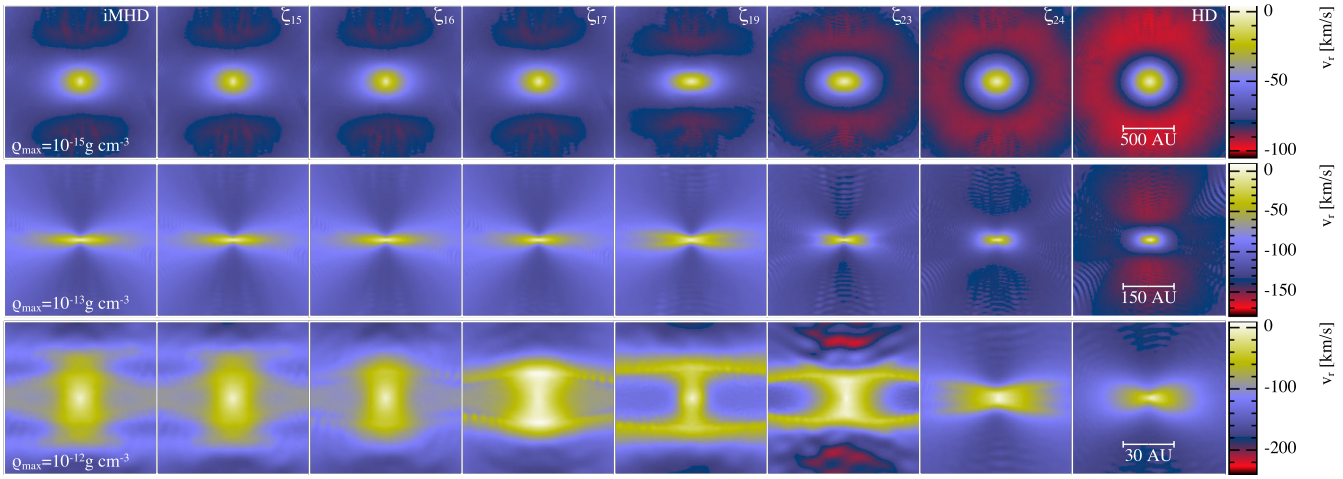

Figure 7. Radial velocity slices through the core of the clouds of selected models as in Fig. 5. The initial radial infall (i.e. where $v_{\rm r} < 0$) is approximately spherical for the low ionization rate models ($\zeta_{\rm cr} \lesssim 10^{-24}$ s^{-1}) and faster at larger radii from the core than for models with higher rates ($\zeta_{\rm cr} > 10^{-24}$ s^{-1}). At larger $\rho_{\rm max}$, the infall becomes less spherical in all models, and the infall rate is faster in the mid-plane for the magnetized models while the vertical infall is faster in HD.

converted into the toroidal magnetic field in ζ_{22} than ζ_{25} (or any other model in our suite). In several models, the maximum toroidal field becomes stronger than the maximum poloidal field at a given location, with $|B_\phi|_{\rm max} > |B_{\rm p}|_{\rm max}$ occurring for ζ_{23}, ζ_{22}, ζ_{20}, ζ_{24}, ζ_{19}, and ζ_{18} at increasing maximum densities.

The maximum magnetic field strength continually increases as the cloud collapses for the models with $\zeta_{\rm cr} \gtrsim 10^{-23}$ s^{-1}, although the growth rate is much slower for ζ_{22} and ζ_{23}. By $\rho_{\rm max} \approx 10^{-13}$ g cm^{-3}, $|B|_{\rm max} \approx 5.7B_0$, $19B_0$, and $130B_0$ for ζ_{23}, ζ_{22}, and iMHD, respectively; the low ionization rate models (i.e. ζ_{24}, ζ_{25}, and ζ_{30}) have magnetic field strengths that asymptote at $|B|_{\rm max} \approx 1.7B_0$.

Fig. 10 shows the evolution of the total kinetic and magnetic energies for selected models. These values include the gas in both the cloud and background medium. Magnetic fields support the molecular cloud against collapse; thus, at any given $\rho_{\rm max}$, there is more kinetic energy in HD than in iMHD, with the kinetic energy decreasing from the HD value to the iMHD value as $\zeta_{\rm cr}$ is increased; this can also be seen in Figs 7 and 8, which show decreasing radial and azimuthal velocities for increasing $\zeta_{\rm cr}$. The total magnetic energy increases for models with $\zeta_{\rm cr} \gtrsim 10^{-22}$ s^{-1}, with the magnetic energy growing more slowly for models with lower $\zeta_{\rm cr}$. The total magnetic energy decreases for the models with $\zeta_{\rm cr} \lesssim 10^{-23}$ s^{-1}; at the end of the simulation, the models with $\zeta_{\rm cr} \lesssim 10^{-24}$ s^{-1} have decreased by $\sim$2 per cent, while ζ_{23} has decreased by only $\sim$0.4 per cent.

4.3 Approaching ideal MHD

As ionization rates increase, the medium becomes more ionized; thus, the ionization fractions begin to approach the ideal MHD limit. However, at temperatures and densities presented here, ionization

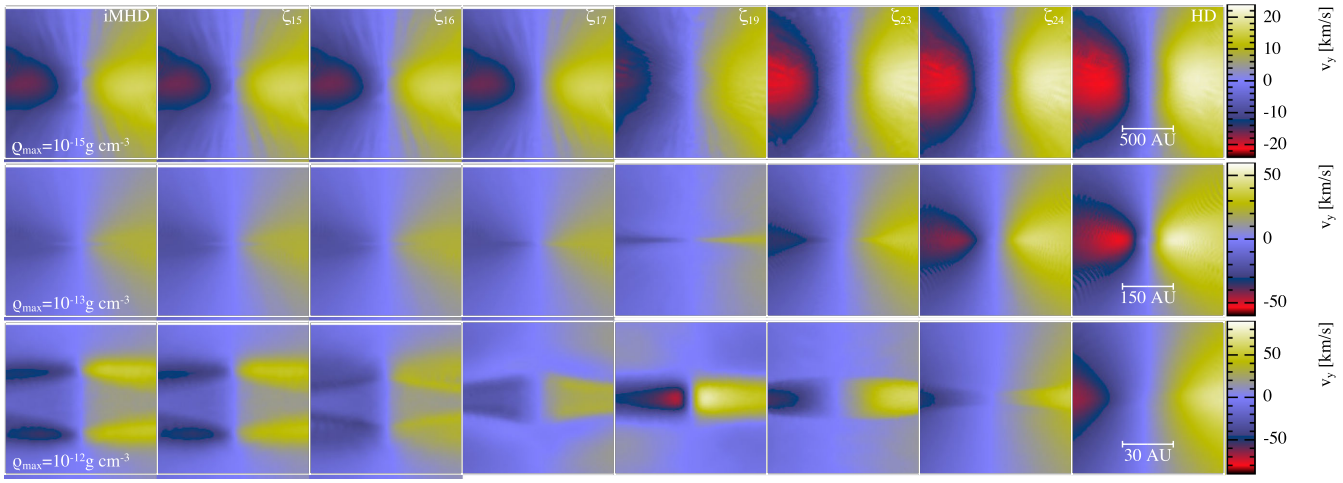

Figure 8. Azimuthal velocity slices through the core of the clouds of selected models as in Fig. 5. The rotation speed of the cloud increases as the cosmic ray ionization rate decreases and as time increases. At $\rho_{\rm max} \approx 10^{-12}$ g cm^{-3}, the rotational speed is faster above and below the disc for $\zeta_{\rm cr} \lesssim 10^{-16}$ s^{-1}; a counter-rotating envelope is beginning to form in ζ_{18} and ζ_{19}.

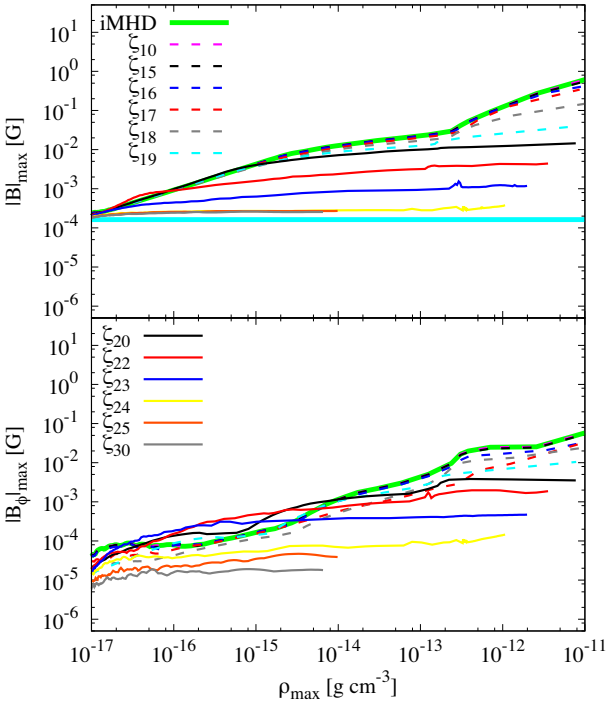

Figure 9. The evolution of the maximum magnetic field strength (top) and the magnitude of the maximum toroidal field $|B_\phi|_{\rm max}$ (bottom) for selected models. The thick cyan line represents the initial magnetic field strength. The legend is split across the panels for clarity. Initially, the entire magnetic field is poloidal $|B_{\rm p}| = \sqrt{B_r^2 + B_z^2}$, and the evolution of the poloidal and total magnetic field strengths are similar. The maximum magnetic field strength increases for all models, although only increases by a factor of ∼1.7 for the low ionization rate models. For the majority of the models, $|B_{\rm p}|_{\rm max} > |B_\phi|_{\rm max}$; however, ζ_{23}, ζ_{22}, ζ_{20}, ζ_{24}, ζ_{19}, and ζ_{18} all switch to having a dominant toroidal field at increasing maximum densities.

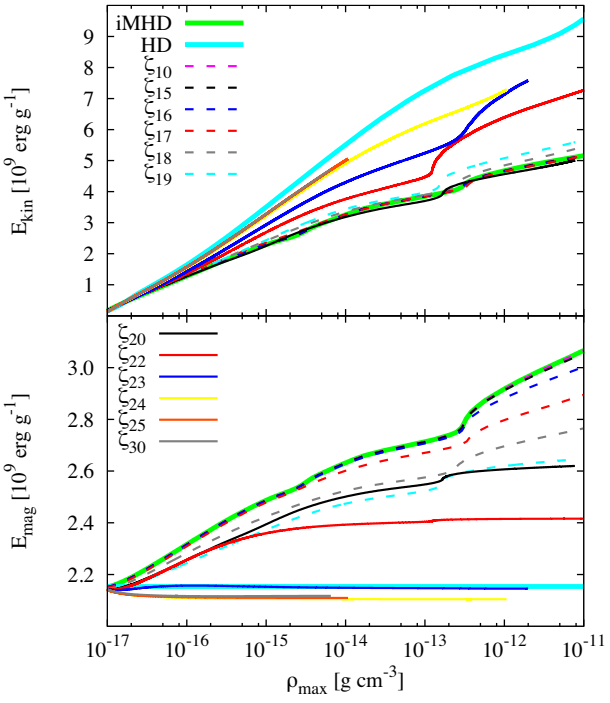

Figure 10. Evolution of the total kinetic (top) and magnetic (bottom) energies for selected models. The thick green and cyan lines represent iMHD and HD, respectively; the thick cyan line in the bottom panel represents the initial magnetic energy, $E_{\rm mag,\,0}$. The legend is split across the panels for clarity. When comparing kinetic energy at similar maximum densities, there is typically a progression from the iMHD to HD models as the ionization rate decreases. For $\zeta_{\rm cr} \gtrsim 10^{-22}$ s^{-1}, the total magnetic energy increases as the molecular cloud collapses, whereas it slightly decreases for $\zeta_{\rm cr} \lesssim 10^{-23}$ s^{-1}.

fraction remains ≪1. The question we ask in this section is how high of an ionization rate is required to safely approximate the ideal MHD limit?

From the induction equation (equation 3), a one-fluid non-ideal MHD system can be approximated as ideal when $\mathrm{d}\boldsymbol{B}/\mathrm{d}t|_{\rm non-ideal} \ll (\boldsymbol{B}\cdot\nabla)\,\boldsymbol{v} - \boldsymbol{B}\,(\nabla\cdot\boldsymbol{v})$. However, we want to know the largest possible $\mathrm{d}\boldsymbol{B}/\mathrm{d}t|_{\rm non-ideal}$ that will still result in a system equivalent to iMHD. Since different quantities may show equivalence at different $\zeta_{\rm cr}$, we will compare several different quantities below, including 2D cross-sections, total and maximum values. A non-ideal MHD model must be equivalent in all of our quantities to be deemed equivalent to iMHD.

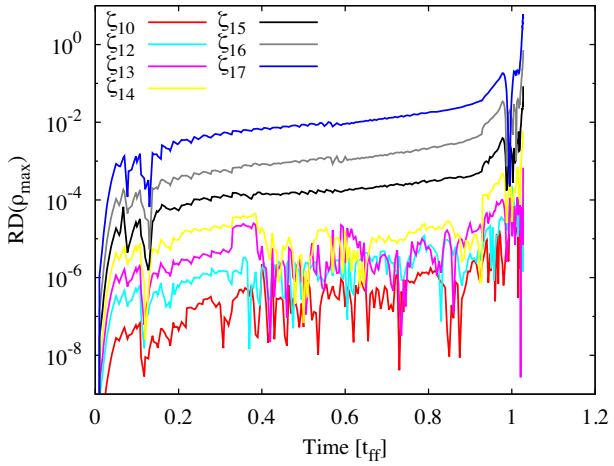

Figure 11. The relative difference, as defined in equation (15), of the maximum density with respect to time for the high ionization rate models compared to iMHD. The relative differences are less than 10 per cent for $t < t_{\rm ff}$; however, even slight differences in evolution times at high densities (i.e. at $t \sim t_{\rm ff}$) cause large relative differences. The evolution times of the models with $\zeta_{\rm cr} \gtrsim 10^{-14}\,{\rm s}^{-1}$ agree within 10^{-4} for the majority of the collapse.

Upon visual inspection of the cross-section plots in Figs 5–8, we find that the models with $\zeta_{\rm cr} \gtrsim 10^{-15}\,{\rm s}^{-1}$ look similar to iMHD for all properties. This also appears true for the evolution of the maximum density with time (Fig. 4) and for total kinetic and magnetic energy (Fig. 10). To quantify this, Fig. 11 shows the relative difference,

$$\mathrm{RD} \equiv \frac{|X\,(\zeta_n) - X\,(\mathrm{iMHD})|}{|X\,(\mathrm{iMHD})|}, \tag{15}$$

where $X(\zeta_n)$ and X(iMHD) are the values for the non-ideal model ζ_n and iMHD, respectively, of the maximum density, $\rho_{\rm max}$, and Fig. 12 shows the relative difference of magnetic energy and total magnetic field strength of a high ionization rate model compared to the iMHD model; for comparison, we intentionally include models that clearly do not approach the ideal limit.

The maximum density in the models with $\zeta_{\rm cr} \gtrsim 10^{-15}\,{\rm s}^{-1}$ differs from iMHD by less than 10 per cent for the entire calculation, with only ζ_{15} yielding a difference larger than 1 per cent near the end.

The relative difference of the magnetic energy and maximum magnetic field strength compared to $\rho_{\rm max}$ decreases for increasing ionization rates; models with higher ionization rates are more similar to iMHD. The magnetic energy of all models with $\zeta_{\rm cr} \gtrsim 10^{-17}\,{\rm s}^{-1}$ differs from iMHD by less than 10 per cent, while the energy in models with $\zeta_{\rm cr} \gtrsim 10^{-15}\,{\rm s}^{-1}$ differs by less than 1 per cent.

Total magnetic energy is a global property of the simulation, including both the quickly collapsing inner region and the slowly evolving background medium. The maximum magnetic field strength, however, is localized in or near the core, and is sensitive to the evolution of the collapse and is obtained from a single particle; thus, we do not expect as low of relative difference as in the energies. Models with $\zeta_{\rm cr} \gtrsim 10^{-12}\,{\rm s}^{-1}$ have maximum magnetic field strengths that differ from iMHD by less than 10^{-4}, while models with $\zeta_{\rm cr} \gtrsim 10^{-14}\,{\rm s}^{-1}$ differ by less than 1 per cent. The relative difference between ζ_{15} and iMHD increases to almost 10 per cent in the first hydrostatic core; this large difference and the increasingly large difference in RD($\rho_{\rm max}$) suggest that ζ_{15} does not approach the ideal MHD limit.

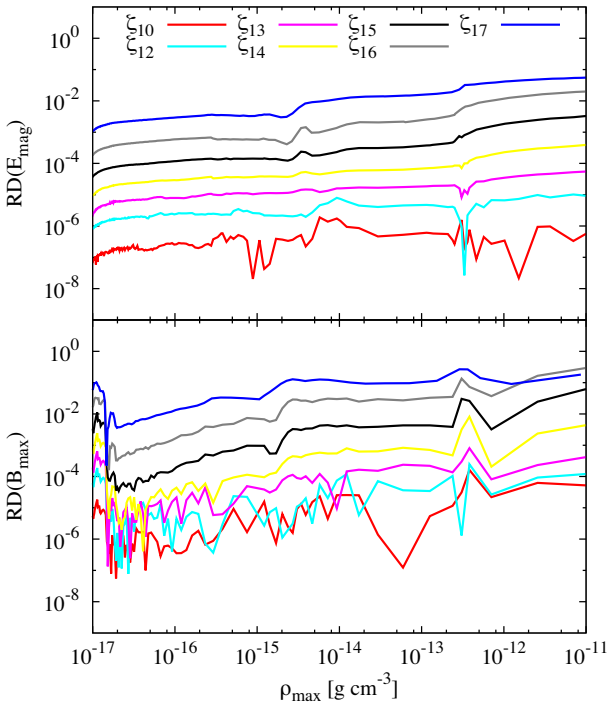

Figure 12. The relative differences of the magnetic energy (top) and the maximum magnetic field strength (bottom) of the high ionization rate models compared to iMHD. For $\rho_{\rm max} \lesssim 10^{-11}\,{\rm g\,cm}^{-3}$, the magnetic energy of the high ionization rate models differs by less than 10 per cent from iMHD, and the maximum magnetic field strength differs by less than 40 per cent.

For $\zeta_{\rm cr} \gtrsim 10^{-14}\,{\rm s}^{-1}$, the grain properties have minimal effect on the non-ideal MHD coefficients (see Section 3.2), except when decreasing to smaller grains of uniform size. Although our conclusions will be qualitatively unaffected by switching to larger grains or to an MRN grain distribution, the agreement between (e.g.) ζ_{14} and iMHD may not be as robust for the smaller grain size of $a_0 = 0.01\,\mu$m.

For the collapse up to $\rho_{\rm max} = 10^{-11}\,{\rm g\,cm}^{-3}$, we conclude that non-ideal MHD models with $\zeta_{\rm cr} \gtrsim 10^{-14}\,{\rm s}^{-1}$ agree with ideal MHD within 1 per cent, and models with $\zeta_{\rm cr} \gtrsim 10^{-13}\,{\rm s}^{-1}$ agree with ideal MHD within 0.1 per cent, suggesting that they are essentially indistinguishable from ideal MHD models.

4.4 Approaching pure hydrodynamics

As ionization rates decrease, the medium becomes more neutral, thus begins to approach the purely hydrodynamic limit. Unlike approaching the ideal limit where all simulations include magnetic fields and non-ideal effects begin to negligibly contribute to their evolution, the hydrodynamic models by definition exclude magnetic fields; thus, for a low ionization rate model to approach the HD model, their evolution must essentially ignore the magnetic field.

In order that the one-fluid non-ideal MHD equations reduce to the ideal MHD limit, all that has to happen is for the third term in equation (3) to become negligible. Thus, it is unsurprising that with a high enough ionization rate, the ideal MHD limit is recovered to a high level of accuracy (see Section 4.3). To recover the hydrodynamical limit, however, all four terms in the induction equation (equation 3), which are calculated using the magnetic field and density of a particle, and its neighbours must sum to exactly zero, and the second term in the momentum equation (equation 2) must also

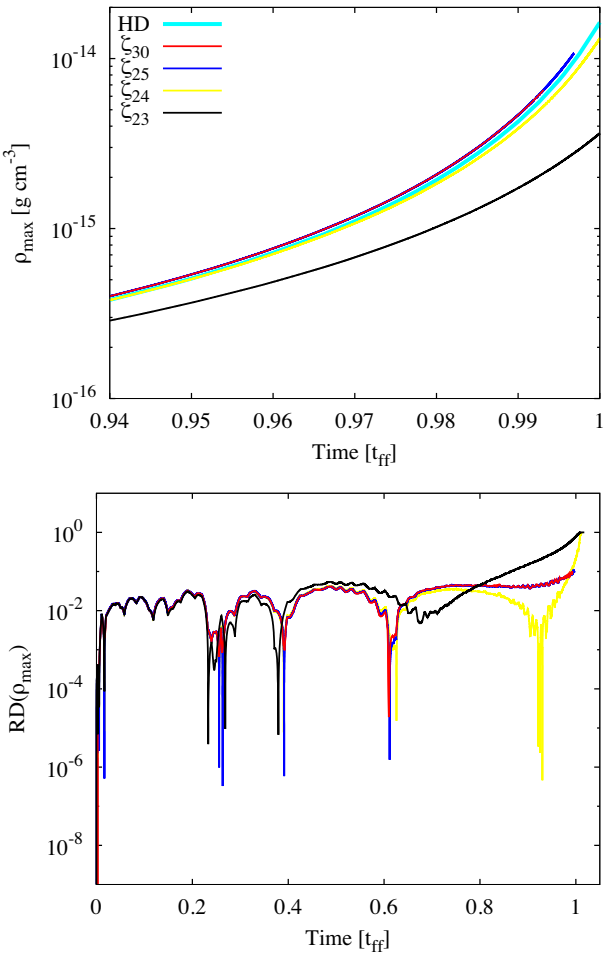

Figure 13. Top: evolution of the maximum density over a short range of time for our low ionization rate models, as in Fig. 4. Bottom: the relative difference of the maximum density with respect to time over the entire evolution, as in Fig. 11. The collapse rates are slightly faster for ζ_{25} and ζ_{30} compared to HD, with the relative difference never surpassing 10 per cent. Model ζ_{24} collapses slightly slower than HD, and the relative difference surpasses 10 per cent at $t \approx 0.99 t_{\rm ff}$.

be zero. Thus, we do not expect to be able to approximate the hydrodynamic limit using non-ideal MHD to the same level of accuracy that was achieved for the ideal limit.

As can be seen in the cross-section plots (Figs 5–8), ζ_{24} shares more characteristics with HD than iMHD or even ζ_{23}; however, there are still noticeable structure differences. Model HD has a slightly larger scale height, and slightly faster rotational and radial velocities. Based upon visual inspection alone, we conclude that by decreasing the ionization rate, the models approach HD; however, ζ_{24} is not equivalent to HD. At $\rho_{\rm max} \approx 10^{-15}$ g cm^{-3}, ζ_{24}, ζ_{25}, and ζ_{30} are indistinguishable from one another, although neither of the latter two models progressed to $\rho_{\rm max} \approx 10^{-13}$ g cm^{-3} for a later comparison.

For our quantitative analysis, Fig. 13 shows $\rho_{\rm max}$ and the relative difference in $\rho_{\rm max}$ of the low ionization rate models compared to HD. The evolution of ζ_{23} has been included for reference, but it clearly cannot approximate HD. The collapse rate for these low ionization rate models varies in time with respect to HD, collapsing slightly faster or slower depending on the time; the transitions are marked by the relative difference approaching zero in these plots. Over the entire evolution, ζ_{24} collapses slower than HD, with the relative difference surpassing 10 per cent by $t \approx 0.99 t_{\rm ff}$. Given the slower collapse and the visual differences, ζ_{24} is not equivalent to HD. Models ζ_{25} and ζ_{30} collapse faster than HD but evolve at the same rate as one another, and at any given time, their maximum density differs from HD by less than 10 per cent.

In ζ_{24}, ζ_{25}, and ζ_{30}, the maximum magnetic field strength grows by a factor of ∼1.7 (bottom panel of Fig. 9); for reference, by this density of $\rho_{\rm max} \approx 5 \times 10^{-15}$ g cm^{-3}, the magnetic field strength in iMHD has increased by a factor of ∼60. Despite the maximum magnetic field strength slightly increasing, the total magnetic energy in these three models decreases to $E_{\rm mag} \approx 0.98 E_{\rm mag,\,0}$ (bottom panel of Fig. 10).

If the grain size was decreased to $a_0 = 0.01$ μm or an MRN distribution was used, then the non-ideal MHD coefficients would be lower; thus, these models would be slightly more ideal (Fig. 2). Therefore, modelling smaller grains would yield low ionization rate models that are even less similar to the hydrodynamical case than those presented here. If an $a_0 = 1$ μm grain size was modelled, then the non-ideal MHD coefficients would be larger, suggesting that these models would be more similar to HD. However, the larger coefficients result in a smaller time-step (recall equation 12), which makes it prohibitively expensive to model; see further discussion in Section 4.5.

Thus, even with low cosmic ray ionization rates of $\zeta_{\rm cr} \lesssim 10^{-24}$ s^{-1}, the relative differences of the energies, magnetic field strengths, and the maximum densities remain between 1 and 10 per cent. However, given the slow growth of the magnetic energy and maximum magnetic field strength, we can conclude that models with $\zeta_{\rm cr} \lesssim 10^{-24}$ s^{-1} approach the hydrodynamic model. At these low ionization rates, unless precision results are required, pure hydrodynamics can be used in place of non-ideal MHD.

4.5 Time-stepping

Given unlimited resources and time, one should simply use non-ideal MHD with the desired cosmic ray ionization rate rather than ideal or hydrodynamic approximations. However, including non-ideal MHD adds to the computational expense both by additional calculations and by decreasing the minimum time-step.

Fig. 14 shows the minimum and CFL time-steps at each density. All models with $\zeta_{\rm cr} \gtrsim 10^{-15}$ s^{-1} have $\mathrm{d}t_{\rm non\text{-}ideal} > \mathrm{d}t_{\rm CFL}$, while ζ_{17} has $\mathrm{d}t_{\rm non\text{-}ideal} \sim \mathrm{d}t_{\rm CFL}$. Models with $10^{-25} \lesssim \zeta_{\rm cr}/\mathrm{s}^{-1} \lesssim 10^{-19}$ are always limited by the Hall time-step, while ζ_{17} and ζ_{18} are Hall-limited for $\rho_{\rm max} \gtrsim 2 \times 10^{-15}$ g cm^{-3} and $\rho_{\rm max} \gtrsim 10^{-16}$ g cm^{-3}, respectively. Model ζ_{30} is limited by the super-time-stepping algorithm using the Ohmic time-step. Note that the ambipolar or Ohmic time-steps would be the limiting case in most models if super-time-stepping were not used.

At $\rho_{\rm max} \approx 10^{-15}$ g cm^{-3}, the non-ideal time-step in ζ_{25} is limited by the Hall time-step and is ∼3900 times shorter than the CFL time-step. At $\rho_{\rm max} \approx 10^{-11}$ g cm^{-3}, the non-ideal time-step in ζ_{17} (which uses the fiducial cosmic ionization ray rate) is ∼15 times shorter than the CFL time-step. Given that studies of collapsing molecular clouds need to reach maximum densities at least a few orders of magnitude larger than presented here, the slow-down of a factor of a few for the canonical ionization rate of $\zeta_{\rm cr} \approx 10^{-17}$ s^{-1} can be tedious, while it can be completely prohibitive for lower ionization rates.

The effect of non-ideal MHD on performance is very evident in the number of CPU hours used, as shown in Fig. 15. The HD model runs ∼53 per cent faster than the iMHD model in part due to the reduced number of calculations required and the slightly longer

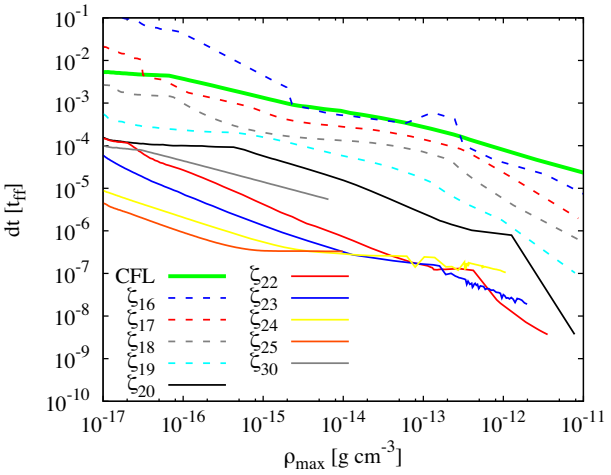

Figure 14. The evolution of the minimum time-step as calculated from the non-ideal terms (see equation 12); the thick green line is the time-step calculated from the CFL condition (see equation 11), and is included for reference. For the models whose time-steps are controlled by Ohmic resistivity or ambipolar diffusion, we plot $\mathrm{d}t = \mathrm{d}t_{\mathrm{OR,\,AD}}/N_{\mathrm{sts}}$, where N_{sts} is given in equation (13). Initially, ζ_{25} requires the smallest time-steps, while ζ_{30} uses a time-step ≈20–50 times larger due to super-time-stepping with the Ohmic time constraint. Models with $\zeta_{\mathrm{cr}} \gtrsim 10^{-15}\,\mathrm{s}^{-1}$ have $\mathrm{d}t_{\text{non-ideal}} > \mathrm{d}t_{\mathrm{CFL}}$, thus are excluded.

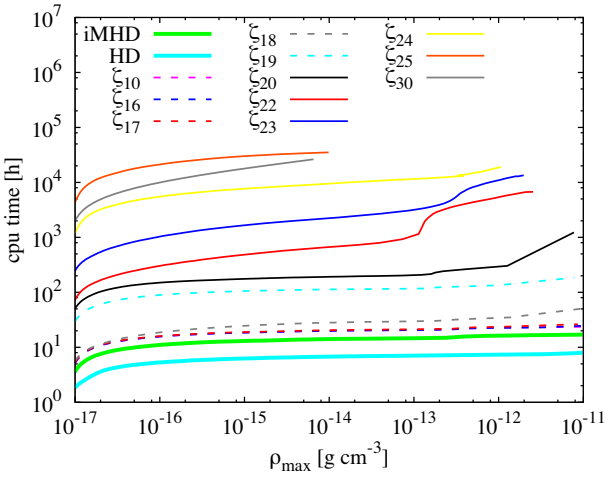

Figure 15. The cumulative CPU time used for each model. HD, iMHD, and models with $\zeta_{\mathrm{cr}} \gtrsim 10^{-18}\,\mathrm{s}^{-1}$ run very quickly to $\rho_{\mathrm{max}} = 10^{-11}\,\mathrm{g\,cm}^{-3}$. As the ionization rate decreases, the required resources become prohibitively expensive, especially for $\zeta_{\mathrm{cr}} \lesssim 10^{-24}\,\mathrm{s}^{-1}$. To reach $\rho_{\mathrm{max}} \approx 10^{-15}\,\mathrm{g\,cm}^{-3}$, it takes $\zeta_{25} \sim 2200$ times longer than iMHD. All the non-ideal models with $\zeta_{\mathrm{cr}} \gtrsim 10^{-17}\,\mathrm{s}^{-1}$ take the same length of time, which is ∼1.4 times longer than iMHD to reach $\rho_{\mathrm{max}} \approx 10^{-11}\,\mathrm{g\,cm}^{-3}$.

CFL time-step since $v_{\mathrm{A}} \equiv 0$. The models with $\zeta_{\mathrm{cr}} \gtrsim 10^{-17}\,\mathrm{s}^{-1}$ take ∼1.4 times longer to reach $\rho_{\mathrm{max}} \approx 10^{-11}\,\mathrm{g\,cm}^{-3}$ than iMHD; since their non-ideal time-steps are similar to the CFL time-step, the additional time used is mostly taken up by the NICIL library. Given that the models with $\zeta_{\mathrm{cr}} \gtrsim 10^{-14}\,\mathrm{s}^{-1}$ well approximate the ideal MHD model (see Section 4.3), an ideal MHD model can instead be run at a speed-up of ∼1.4.

As the ionization rate decreases, the cumulative CPU time increases, with ζ_{25} being the most expensive simulation followed by ζ_{30} and then the remainder of the models in order of increasing ionization rate. To reach $\rho_{\mathrm{max}} \approx 10^{-15}\,\mathrm{g\,cm}^{-3}$, it takes ζ_{25} ∼2200 times longer than iMHD; thus, these models are prohibitively expensive to run to any useful maximum density. However, since the models with $\zeta_{\mathrm{cr}} \lesssim 10^{-24}\,\mathrm{s}^{-1}$ have small relative differences for their total magnetic energies and maximum magnetic field strengths, respectively, it would be reasonable to run purely hydrodynamical models in their place.

5 SUMMARY AND CONCLUSION

We have presented a suite of non-ideal MHD simulations with various cosmic ray ionization rates ζ_{cr} to determine what rate is required to recover a hydrodynamical collapse and an ideal MHD collapse. Our models were initialized as a 1 $\mathrm{M}_{\odot}$, spherically symmetric, rotating molecular cloud core; the cloud was magnetized with a magnetic field initially aligned anti-parallel to the rotation axis, and had an initial strength of $B_0 = 1.63 \times 10^{-4}\,\mathrm{G}$, or $\mu_0 = 5$. Our models used a uniform grain size of $a_0 = 0.1\,\mu\mathrm{m}$, but we discussed how different grain models are expected to change the results. In particular, we found that at high cosmic ray ionization rates, the results will be approximately independent of grain properties, but at very low ionization rates the non-ideal MHD coefficients that we use tend to be larger than those produced by MRN grain size distributions, suggesting that the ionization rates required to approximate hydrodynamical evolution may be even lower than the values we find using $a_0 = 0.1\,\mu\mathrm{m}$. All three non-ideal MHD terms (Ohmic resistivity, Hall effect, and ambipolar diffusion) were included. We tested 15 different cosmic ray ionization rates, which were held constant for the entire simulation. The initial density of the molecular cloud core was $\rho_0 = 7.43 \times 10^{-18}\,\mathrm{g\,cm}^{-3}$, and it was evolved until $10^{-15} \lesssim \rho_{\mathrm{max}}/(\mathrm{g\,cm}^{-3}) \lesssim 10^{-11}$, depending on the value of ζ_{cr}.

Our two key results are as follows.

(i) *Approaching the ideal MHD limit*: We evolved models with high ionization rates until they entered the first hydrostatic core and reached $\rho_{\mathrm{max}} \approx 10^{-11}\,\mathrm{g\,cm}^{-3}$. Models with $\zeta_{\mathrm{cr}} \gtrsim 10^{-13}\,\mathrm{s}^{-1}$ were indistinguishable from the ideal MHD model when considering the evolution of their maximum density, magnetic energy, and magnetic field strengths, i.e. all properties matched the evolution of the ideal MHD model within 0.1 per cent. The evolution of the model with $\zeta_{\mathrm{cr}} = 10^{-14}\,\mathrm{s}^{-1}$ matched the evolution of the ideal MHD model within 1 per cent.

(ii) *Approaching the hydrodynamic limit*: The models with $\zeta_{\mathrm{cr}} \lesssim 10^{-24}\,\mathrm{s}^{-1}$ look similar to the hydrodynamical model, but with noticeable differences; in these models, the total magnetic energy grew by a factor of 1.7 and the maximum magnetic field strength decreased by 2 per cent. Our lowest ionization rate models were not followed beyond the isothermal collapse phase due to the non-ideal MHD constraints on the time-step. Those with $\zeta_{\mathrm{cr}} \lesssim 10^{-25}\,\mathrm{s}^{-1}$ had maximum densities at a given time that agreed with the hydrodynamical model within 10 per cent. Given the reasonable agreement with the hydrodynamical model and the orders of magnitude increase in runtime, we conclude that hydrodynamical models can be used to approximate non-ideal MHD models with $\zeta_{\mathrm{cr}} \lesssim 10^{-24}\,\mathrm{s}^{-1}$ unless precision results are required.

We conclude that it is possible to reproduce ideal MHD and purely hydrodynamical collapses using non-ideal MHD given an appropriate cosmic ray ionization rate. However, reaching either limit by cosmic ray ionization alone is unlikely, since molecular clouds in the local neighbourhood have cosmic ray ionization rates of $\zeta_{\mathrm{cr}} \approx 10^{-17}\,\mathrm{s}^{-1}$ (e.g. Padovani, Galli & Glassgold 2009; Neufeld & Wolfire 2017). Even if the comic ray ionization rate were to temporarily increase (e.g. due to a nearby supernova), the

increase will not be sustained enough to shift the evolution into the ideal MHD regime for the lifetime of the initial collapse.

For cosmic ray ionization rates of $\zeta_{\rm cr} \lesssim 10^{-24}\,{\rm s}^{-1}$, we can approximate a hydrodynamic collapse; however, it is improbable to reach these low ionization rates in local diffuse molecular clouds given that this rate is well below the rate expected from radionuclide decay. Studies of the early Universe by Susa, Doi & Omukai (2015) found that, even in the absence of cosmic rays and heavy metals, the primordial gas is partially ionized (i.e. contains e^-, H^+, Li^+). Their electron fractions for this case are similar to ours for $\zeta_{\rm cr} \lesssim 10^{-24}\,{\rm s}^{-1}$; however, their H^+, Li^+ fractions are higher due to the absence of dust grains. Although our low ionization rate models are unlikely to be relevant in the local Universe, they may have implications for the early Universe.

While our quantitative conclusions depend on our initial conditions and our chosen maximum densities, we find that the canonical cosmic ray ionization rate of $\zeta_{\rm cr} = 10^{-17}\,{\rm s}^{-1}$ approaches neither the ideal MHD limit nor the hydrodynamical limit. For star formation simulations to properly evolve the magnetic field, non-ideal MHD is essential.

ACKNOWLEDGEMENTS

JW and MRB acknowledge support from the European Research Council under the European Community's Seventh Framework Programme (FP7/2007- 2013 grant agreement no. 339248). DJP received funding via Australian Research Council grants FT130100034, DP130102078, and DP180104235. This work was supported by resources on the swinSTAR national facility at Swinburne University of Technology. swinSTAR is funded by Swinburne and the Australian Government's Education Investment Fund.

REFERENCES

Alexiades V., Amiez G., Gremaud P.-A., 1996, Commun. Numer. Methods Eng., 12, 31
Asplund M., Grevesse N., Sauval A. J., Scott P., 2009, ARA&A, 47, 481
Bate M. R., Tricco T. S., Price D. J., 2014, MNRAS, 437, 77
Bourke T. L., Myers P. C., Robinson G., Hyland A. R., 2001, ApJ, 554, 916
Braiding C. R., Wardle M., 2012a, MNRAS, 422, 261
Braiding C. R., Wardle M., 2012b, MNRAS, 427, 3188
Choi E., Kim J., Wiita P. J., 2009, ApJS, 181, 413
Ciolek G. E., Mouschovias T. C., 1994, ApJ, 425, 142
Commerçon B., Hennebelle P., Audit E., Chabrier G., Teyssier R., 2010, A&A, 510, L3
Crutcher R. M., 1999, ApJ, 520, 706
Dapp W. B., Basu S., 2010, A&A, 521, L56
Dapp W. B., Basu S., Kunz M. W., 2012, A&A, 541, A35
Draine B. T., Lee H. M., 1984, ApJ, 285, 89
Duffin D. F., Pudritz R. E., 2009, ApJ, 706, L46
Fiedler R. A., Mouschovias T. C., 1993, ApJ, 415, 680
Gammie C. F., 1996, ApJ, 457, 355
Heiles C., Crutcher R., 2005, in Wielebinski R., Beck R., eds, Lecture Notes in Physics, Vol. 664, Cosmic Magnetic Fields. Springer-Verlag, Berlin, p. 137
Hennebelle P., Ciardi A., 2009, A&A, 506, L29
Hennebelle P., Fromang S., 2008, A&A, 477, 9
Igea J., Glassgold A. E., 1999, ApJ, 518, 848
Keith S. L., Wardle M., 2014, MNRAS, 440, 89
Krasnopolsky R., Li Z.-Y., Shang H., Zhao B., 2012, ApJ, 757, 77
Kunz M. W., Mouschovias T. C., 2009, ApJ, 693, 1895
Larson R. B., 1969, MNRAS, 145, 271
Larson R. B., 1972, MNRAS, 156, 437
Li Z.-Y., Shu F. H., 1996, ApJ, 472, 211
Li Z.-Y., Krasnopolsky R., Shang H., 2011, ApJ, 738, 180
Mac Low M.-M., Norman M. L., Konigl A., Wardle M., 1995, ApJ, 442, 726
Machida M. N., Inutsuka S.-I., Matsumoto T., 2011, PASJ, 63, 555
Mathis J. S., Rumpl W., Nordsieck K. H., 1977, ApJ, 217, 425
Mellon R. R., Li Z.-Y., 2009, ApJ, 698, 922
Mestel L., Spitzer L., Jr, 1956, MNRAS, 116, 503
Meyer C. D., Balsara D. S., Aslam T. D., 2012, MNRAS, 422, 2102
Mouschovias T. C., 1996, in Tsinganos K. C., Ferrari A., eds, NATO Advanced Science Institutes (ASI) Series C Vol. 481. Springer-Verlag, Netherlands, p. 505
Mouschovias T. C., Ciolek G. E., 1999, in Lada C. J., Kylafis N. D., eds, NATO Advanced Science Institutes (ASI) Series C Vol. 540. Springer-Verlag, Netherlands, p. 305
Mouschovias T. C., Spitzer L., Jr, 1976, ApJ, 210, 326
Nakano T., Umebayashi T., 1986a, MNRAS, 218, 663
Nakano T., Umebayashi T., 1986b, MNRAS, 221, 319
Nakano T., Nishi R., Umebayashi T., 2002, ApJ, 573, 199
Neufeld D. A., Wolfire M. G., 2017, ApJ, 845, 163
O'Sullivan S., Downes T. P., 2007, MNRAS, 376, 1648
Padovani M., Galli D., Glassgold A. E., 2009, A&A, 501, 619
Pandey B. P., Wardle M., 2008, MNRAS, 385, 2269
Pollack J. B., Hollenbach D., Beckwith S., Simonelli D. P., Roush T., Fong W., 1994, ApJ, 421, 615
Price D. J., 2012, J. Comput. Phys., 231, 759
Price D. J., Bate M. R., 2007, MNRAS, 377, 77
Price D. J., Monaghan J. J., 2004, MNRAS, 348, 123
Price D. J., Monaghan J. J., 2005, MNRAS, 364, 384
Price D. J. et al., 2017, PASA, preprint (arXiv:1702.03930)
Seifried D., Banerjee R., Klessen R. S., Duffin D., Pudritz R. E., 2011, MNRAS, 417, 1054
Shu F. H., Galli D., Lizano S., Cai M., 2006, ApJ, 647, 382
Spitzer L., Tomasko M. G., Jr, 1968, ApJ, 152, 971
Susa H., Doi K., Omukai K., 2015, ApJ, 801, 13
Tassis K., Mouschovias T. C., 2007, ApJ, 660, 370
Tomida K., Tomisaka K., Matsumoto T., Hori Y., Okuzumi S., Machida M. N., Saigo K., 2013, ApJ, 763, 6
Tomida K., Okuzumi S., Machida M. N., 2015, ApJ, 801, 117
Tricco T. S., Price D. J., 2012, J. Comput. Phys., 231, 7214
Tricco T. S., Price D. J., Bate M. R., 2016, J. Comput. Phys., 322, 326
Troland T. H., Crutcher R. M., 2008, ApJ, 680, 457
Tscharnuter W. M., 1987, A&A, 188, 55
Tsukamoto Y., Iwasaki K., Okuzumi S., Machida M. N., Inutsuka S., 2015a, ApJ, 810, L26
Tsukamoto Y., Iwasaki K., Okuzumi S., Machida M. N., Inutsuka S., 2015b, MNRAS, 452, 278
Tsukamoto Y., Okuzumi S., Iwasaki K., Machida M. N., Inutsuka S.-i., 2017, PASJ, 69, 95
Turner N. J., Sano T., 2008, ApJ, 679, L131
Umebayashi T., Nakano T., 1981, PASJ, 33, 617
Umebayashi T., Nakano T., 1990, MNRAS, 243, 103
Umebayashi T., Nakano T., 2009, ApJ, 690, 69
Wardle M., 2007, Ap&SS, 311, 35
Wardle M., Ng C., 1999, MNRAS, 303, 239
Wurster J., 2016, PASA, 33, e041
Wurster J., Price D., Ayliffe B., 2014, MNRAS, 444, 1104
Wurster J., Price D. J., Bate M. R., 2016, MNRAS, 457, 1037
Wurster J., Bate M. R., Price D. J., Tricco T. S., 2017a, Crespo A. J. C., Gesteira M. G., Altomare C., eds, Proc. SPHERIC 2017: 12th International SPHERIC Workshop. Universidade de Vigo, Spain
Wurster J., Price D. J., Bate M. R., 2017b, MNRAS, 466, 1788
Wurster J., Bate M. R., Price D. J., 2018, MNRAS, 475, 1859

This paper has been typeset from a TEX/LATEX file prepared by the author.